Investigation of sources of gravity waves observed in the Brazilian Equatorial region on 08 April 2005

Oluwakemi Dare-Idowu[1,2], Igo Paulino[1], Cosme A. O. B. Figueiredo[3], Amauri F. Medeiros[1], Ricardo A. Buriti[1], Ana Roberta Paulino[1,4], and Cristiano M. Wrasse[3]

[1]Unidade Acadêmica de Física, Universidade Federal de Campina Grande, Campina Grande, Brazil.
[2]University of Paul Sabatier, Toulouse, France
[3]Divisão de Aeronomia, Instituto Nacional de Pesquisas Espaciais, São José dos Campos, Brazil
[4]Departamento de Física, Universidade Estadual da Paraíba, Campina Grande, Brazil

Correspondence: Oluwakemi Dare-Idowu (oluwakemidareidowu@gmail.com)

Abstract.

On 08 April 2005, a strong gravity wave activity (of more than 3 hours) was observed in São João do Cariri (7.4° S, 36.5° W). These waves propagated to the southeast and presented different spectral characteristics (wavelength, period and phase speed). Using the hydroxyl (OH) airglow images, the characteristics of the observed gravity waves were calculated; the wavelengths ranged between 90 and 150 km, the periods from ~26 to 67 min and the phase speeds ranged from 32 to 71 m/s. A reverse ray-tracing analysis was performed to research the possible sources of these detected waves. The ray-tracing database was composed of temperature profiles from NRLMSISE-00 model and SABER measurements and wind profiles from HWM model and meteor radar data. According to the ray path, the likely source of these observed gravity waves was the Inter Tropical Convergence Zone with intense convective processes taking place in the northern part of the observatory. Also, the observed preferential propagation direction of the waves to the southeast could be explained using blocking diagrams, i.e. due to the wind filtering process.

Keywords. Gravity waves, Airglow, Reverse Ray Tracing, Troposphere, Mesosphere, ITCZ.

1. Introduction

Since the publication of the pioneering works of Hines in the 1960s on the detection of irregular motions 'gravity waves' in the upper atmosphere, there have been numerous improvement work-outpours. Gravity waves are results of disturbances that occur in atmospheric fluids with the upper mesosphere and thermosphere region being largely impacted (e.g., Fritts and Alexander, 2003). Potential sources of these waves are cold fonts (e.g Plougonven et al., 2017), troposphere convection (e.g., Vadas et al., 2009), wind shear (e.g Clemesha and Batista, 2008), topography and wave breaking (e.g., Sarkar and Scotti, 2017), as well as solar eclipse (e.g., Marlton et al., 2016). These atmospheric structures have been identified as a key component in the transportation of energy in the mesosphere and lower thermosphere (MLT) region (e.g., Fritts, 1993; Medeiros et al., 2007; Campos et al., 2016).

Internal GWs are generated as adjustment radiations whenever a sudden change in forcing causes the atmosphere to depart from its large-scale balanced state. Such a forcing anomaly occurs during a solar eclipse (Campos et al., 2016; Marlton et al., 2016). The intrinsic properties of the gravity waves (observed horizontal phase speed, propagation direction, observed period, horizontal wavelength) can be calculated directly from the airglow images by spectral analyzing. Using the dispersion relation, the vertical wavelength can also be computed (Vargas et al., 2009). Gravity waves can be summarized as large-scale waves, medium-scale waves, and small-scale waves. Small-scaled gravity waves are characterized by horizontal wavelengths in tens of kilometers (Medeiros et al., 2003), medium-scaled gravity waves propagate at ~ 170 km altitude, and large-scale waves have high phase speeds and travel farther horizontal distances compared to others (Vadas et al., 2009).

In the MLT region, there are several and continuous chemical reactions such as the OH airglow emissions (e.g., Sivjee et al., 1992; Taylor et al., 2009; Campos et al., 2016). These emissions among several others have been used by many authors as a proxy for investigating gravity wave activities. Airglow emissions are faint luminescence that are produced as a result of the emission of solar radiations (ultraviolet and x-radiation) by ionized air molecules. These luminosity are usually captured by the all sky imagers (ASI) (e.g., Chamberlain, 1954; Krasovskij et al., 1965).

To identify source location of gravity waves, the reverse ray tracing method has been widely adopted. This algorithm allows the identification of the source locations of gravity waves. Several researchers have successfully implemented this technique to identify points of generation of these waves under different atmospheric conditions using airglow images (e.g., Hecht et al., 1994; 1997; Brown et al., 2004; Wrasse et al., 2006; Vadas et al., 2009; Pramitha et al., 2014, Sivakandan et al., 2016).

Wrasse et al., (2006) did a comprehensive study of gravity waves observed over Brazil and Indonesia and concluded that most of the studied waves have their sources in the troposphere. Similarly, Vadas et al. (2009) studied the propagation of gravity waves observed during the SpreadFEx campaign in Brazil and found out that the likely sources of those waves were deep convection in Brazil. In addition, Pramitha et al., (2014) identified that 64 % of observed GWs over Gadanki, India originated from the upper troposphere while the remaining were seen to have been ducted in the mesosphere. Furthermore, in 2016, Sivakandan et al. (2016) studied Gws observed in the southern part of India and associated the sources to convection.

The objective of this current study is to extensively study a strong activity of GWs observed in São João do Cariri (7.4º S, 36.5º W) on 08 April 2005. More than three hours of GW activities were observed and the waves propagated exclusively to the southeast. An explanation for this uncommon pattern is presented in this work investigating the combining effect of the location of the source and the wind filtering process.

2. Instrumentation

2.1 The all sky imager

The GWs detected in this study were observed using the ASI installed at the observatory in São João do Cariri. The ASI is an optical instrument that provides monochromatic maps of aurora and atmospheric airglow emission of different wavelengths. It has been designed to keep track of the spatial and temporal variations of OH, OI5577, 6300 nm airglow emissions (e.g. Paulino et al., 2010).

This present study however utilized only the OH airglow images captured by the ASI at an altitude of 87 km. This instrument comprises of a fish-eye (f/4) lens, a telecentric lens system, a field of view of 180^0, a computer-controlled filter wheel with several slots for the observation of different emissions, and a charged coupled device (CCD) camera with a CCD device used as a photodetector for increased sensitivity. More technical and operational details about this particular imager at São João do Cariri can be found in Medeiros et al., 2007; Paulino et al. (2012).

2.2 TIMED/SABER Satellite

The Sounding of the Atmosphere using Broadband Emission Radiometry (SABER) is one of the four instruments onboard the Thermosphere Mesosphere Ionosphere Energetics and Dynamics (TIMED) satellite. This instrument measures the vertical temperature profile of the atmosphere. In this study, at 7.4º S, 36.5º W, the vertical temperature measurements from 20 to 108 km were obtained from SABER. Data from the Naval Research Laboratory Mass-Spectrometer-Incoherent-Scatter (NRLMSISE00) atmospheric model (Picone et al., 2002) was utilized for complementing the measurements at unavailable heights of 0-19 km, and 109-400 km. These measurements were used to provide vertical profiles of kinetic temperature, pressure, geopotential height, and volume mixing ratios for the trace species (Mertens et al., 2001).

2.3 The SKiYMET Meteor Radar

The All-Sky Interferometric Meteor Radar (SKiYMET) system located at 7.4º S, 36.5º W provided measurements of the horizontal wind speeds and direction of the mesosphere (81-99 km). The radar which is composed of Yagi antennas-5 receiving antennas and one transmitting antenna operates at 35.24 MHz with a maximum power of 12 kW. This instrument detects the trail left behind by vaporized meteors, determines the angle-of-arrival by using the phase difference between the receiving antennas, then measures the radial velocity by using the derivation of the speed and direction of the atmospheric winds carrying the meteor trail at a specified altitude. The phase delay between the transmitted and received signal is used to determine the position of the trail. Further detail about this radar has been published in (e.g., Hocking et al., 2001; Egito et al., 2018; Paulino et al., 2015).

3. Methodology and data analysis

3.1 Determination of gravity waves parameters

To obtain the characteristics of the detected gravity waves, a two- dimensional Fast Fourier Transform (FFT) was used in specified batches of OH airglow images. The pre-processing of the airglow images can be summarized in the following procedures:

- Rotating the image to fit the top of the image with the north geographic region;
- Removing low frequency waves by applying the Butterworth high pass filter;
- Contrast enhancement and unwarping the airglow images for FFT analysis.

Figure 1(a) shows one of the raw OH image obtained from the ASI in Observatorio de Luminescencia Atmosferica de Paraiba (OLAP). This image is a typical example of the wave events observed on this night. The ripples enclosed in the red box in Figure (1a) represents the gravity wave structure. This particular event was captured by the ASI at ~23:58 UT on 08 April 2005. This image however was contaminated with stars (bright circles), and the Milky Way (white streak running from the bottom North-West to South-East direction), tree branches/leaves (East-edge of the image), and building tops shown by the red arrow. Figure 1(b) portrays a clearer image after image processing. Figure 1(c) represents the unwarped version of previous image. The last figure shows the spectrum of the encapsulated event. The bright red circle which depicts the amplitude of the gravity wave and its positioning also provides the propagating direction of the wave. Table 1 presents a summary of all the wave events observed on this night. Additional information about the cross spectrum analysis used in this present study to obtain the characteristics of these waves can be found in (Wrasse et al., 2007).
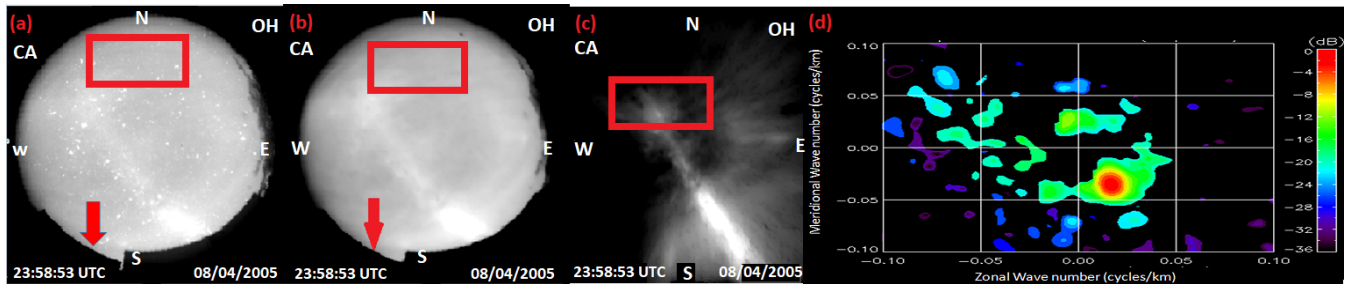
Figure 1: Illustration of the image processing. (a) Raw OH image collected from the ASI in São João do Cariri on 08 April 2005 (b) Filtered image (c) Unwarped and rotated image of the gravity wave event inside the red box area in previous images for FFT analysis (d) Cross spectrum applied to the GW enclosed in the box in (c).

Table 1: The observed properties of the 5 wave events

Event	Time (UTC)	τ (min)	λ_H (km)	Propagation direction (^{o})	cH (ms−1)
01	20:22	26.3	90.2	139.8	57.2
02	21:33	66.9	144.5	131.2	36.0
03	22:56	64.2	125.8	125.0	32.7
04	23:29	40.8	142.0	142.0	58.0
05	23:58	35.0	149.2	150.9	71.0

3.2 The atmospheric profile

The SABER instrument provided temperature measurement from 23h46 to 23h51 UT on 08 April, and from 08h35 to 08h40 UT on 09 April for altitudes 20-108 km. Then, linear interpolation between 23h46 (08 April) and 08h40 (09 April) was done for the same altitude range. In addition, numerical values for temperature were obtained from https://omniweb.gsfc.nasa.gov/vitmo/msis_vitmo.html for time (12h to 22h) on 08 April 2005 and for missing heights of (0-19km, 109-400km) to complement the SABER measurements. Finally, a 13-profile temperature data with a temporal resolution of 2hrs was constructed for the whole period. However, some discrepancies were at the combining points, hence the data were smoothened so that the model can seamlessly match the measurements at these junctions. This methodology was discussed by Paulino et al. (2012). The temporal and spatial variation of the temperature (not shown) with a contour interval of 154 km reveals an outbreak of cold air at heights lesser than 150 km (< 300K). The peak period between 17h00 and 19h00 has a temperature value 1000 K.

The SKYiMET radar provided the zonal and meridional wind measurements from 81-99 km every 3 km from 0h to 23h on 08 and 09 April 2005 with a resolution of 1h. Similarly, numerical interpolation provided the spatial resolution of the wind with a 2 hours resolution like the temperature- with supporting data from the Horizontal Wind Model (HWM) (Drob et al., 2008) from 0 km to 80 km, and above 100 km.

From the temperature and wind measurements, other atmospheric parameters representing the atmospheric state of the period of study were obtained. The pressure $P(z) = P_o \exp\left(-\int_0^z \frac{g}{RT} dz'\right)$ was obtained using a combination of the ideal gas law $P = R\rho T$ and the hydrostatic balance equation $\frac{dP}{dz} = -gp$ where ρ is the density obtained from https://omniweb.gsfc.nasa.gov/vitmo/msis_vitmo.html, and the molecular weight was estimated from

$$X_{MW} = \frac{1}{2}\left(X_{MW0} - X_{MW1}\right)\left[1 - \tanh\frac{s-a}{\Delta_a}\right] + X_{MW1}$$ where X_{MW0}, X_{MW1}, Δ_a and a are constants given by 28.90, 16.0, 4.20, and 14.90 respectively, while $s = ln\rho$ (Vadas et al., 2009). Additional details about the reverse-ray tracing parameters can be found in (Vadas et al., 2007; Vadas et al., 2009), T is the temperature, **g** is the acceleration due to gravity, $R = \frac{8314.5}{X_{MW}}$ is the gas constant, z is the altitude, and P_o is the static pressure.

The scale height $H = -\rho / d\rho / dz$ is obtained from the ratio of the density to the derivative with respect to the altitude, while the potential temperature is $\theta = T \left(P_o / P \right)^{R/C_p}$, C_p is the specific heat capacity at constant pressure, and the

135 Brunt–Väisälä frequency is $N = \sqrt{\left(\dfrac{g}{\Theta} \dfrac{d\Theta}{dz} \right)}$. See further details in Vadas et al., (2007).

3.3 The Reverse Ray Tracing technique

Every gravity waves gets influenced by the atmospheric winds with velocity **V** = (U, V, W) according to the following equations: Equation 1 describes the ray path while the refraction of the wave vector along the ray path is explained 140by equation 2.

$$\frac{dx_i}{dt} = -k_j \frac{\partial V_j}{\partial x_i} - \frac{\partial \omega_{Ir}}{\partial x_i} \tag{1}$$

and

$$\frac{(dk_i)}{dt} = -V_i + \frac{(\partial \omega_{ir})}{k_i} = -V_i + c_{gi} \tag{2}$$

U, V, W, are the zonal, meridional, and vertical wind components respectively, x_i is the spatial position of the wave 145according to the spatial component $'i'$, ω_{Ir} is the real part of the intrinsic frequency obtained using the dispersion relation in Equation 40 and Equation 48 of Vadas and Fritts, 2004, k is the wave number, and c_g is the group velocity. The derivatives of the group velocities and the complete dispersion relation can be found in Vadas and Fritts (2005) and Vadas (2007).

Considering 3D-space, the wave trajectory can be represented using the dispersion relation as (3a-3c), also, the refraction of the wave packages can be represented as (3d-3f). Numerical integration of the six ordinary differential 150equations (3a-3d) was performed using Runge-Kutta fourth order (Press, 2007). All the observed and intrinsic properties of the gravity waves and parameters representing the atmospheric condition were fed into the reverse ray-tracing (RRT) model. The four stopping conditions imposed constantly checks the horizontal phase speed with the background winds. When any of the condition is violated, the ray tracing integration is terminated. The main stopping criteria are: (i) if the group velocity of the gravity wave is close to the speed of sound ($c_g >= 0.9 c_s$); (ii) when the real part of the intrinsic frequency tends to zero 155($w_{Ir} \rightarrow 0$); (iii) when the vertical wavelength is greater than viscosity length or dissipation of the gravity waves. (iv) If the momentum flow of the gravity wave $u_{GW} w_{GW}(z,t) \geq 10^{-5} u_{GW} w_{GW}$ at the height of OH airglow (87km). Extensive detail of the reverse ray tracing algorithm employed in this study has been published by Paulino et al., 2012; and Pramitha et al., 2014.

$$\frac{dx}{dt} = U + \frac{k(N^2 - \omega_{Ir}^2)}{\omega_{Ir} \Delta} \tag{3a}$$

$$160 \frac{dy}{dt} = V + \frac{l(N^2 - \omega_{Ir}^2)}{\omega_{Ir} \Delta} \tag{3b}$$

$$\frac{dz}{dt} = \frac{-m(\omega_{Ir}^2 - f^2)}{\omega_{Ir} \Delta} \tag{3c}$$

$$\frac{dk}{dt} = -k \frac{\partial U}{\partial x} - l \frac{\partial V}{\partial x} - \frac{1}{2\omega_{Ir} \Delta} \left[\frac{\partial N^2}{\partial x}(k^2 + l^2) - \frac{\partial \alpha^2}{\partial x}(\omega_{Ir}^2 - f^2) \right] \tag{3d}$$

$$\frac{dl}{dt} = -k \frac{\partial U}{\partial y} - l \frac{\partial V}{\partial y} - \frac{1}{2\omega_{Ir} \Delta} \left[\frac{\partial N^2}{\partial y}(k^2 + l^2) - \frac{\partial \alpha^2}{\partial x}(\omega_{Ir}^2 - f^2) \right] - \frac{f}{\omega_{Ir} \Delta} \frac{df}{dy}(m^2 + \alpha^2) \tag{3e}$$

$$\frac{dm}{dt} = -k \frac{\partial U}{\partial z} - l \frac{\partial V}{\partial z} - \frac{1}{2\omega_{Ir} \Delta} \left[\frac{\partial N^2}{\partial z}(k^2 + l^2) - \frac{\partial \alpha^2}{\partial z}(\omega_{Ir}^2 - f^2) \right] \tag{3f}$$

where $\Delta = k^2 + l^2 m^2 + \alpha^2$ and $\alpha = \frac{1}{2}H$, *k, l*, and *m* represents the zonal, meridional, and vertical wave numbers, and H is the density scale height (Vadas and Fritts, 2005; Pramitha et al., 2014),

4. Results and discussions

4.1 Spectral Analysis Result

170   The spectral results shown in Table 1 shows that the observed wavelengths have a standard deviation of 24 km and mean value of 130 km with a large amount of variability among the detected waves. This result agrees with the reports of Medeiros et al., (2007) for waves detected at this observatory. Thus, it can be confidently concluded that the observed wavelengths are good representatives of the gravity waves in this observatory.

      Figure 2 shows the traveling direction of the 5 events. From the polar chart, it is seen that all the waves are 175 propagating Southeast with an approximate azimuth of ~134° from the north. This is in favorable agreement with the results obtained from previous studies for the same observatory (Essien et al. 2018). This anisotropicity will be discussed later on in this study.
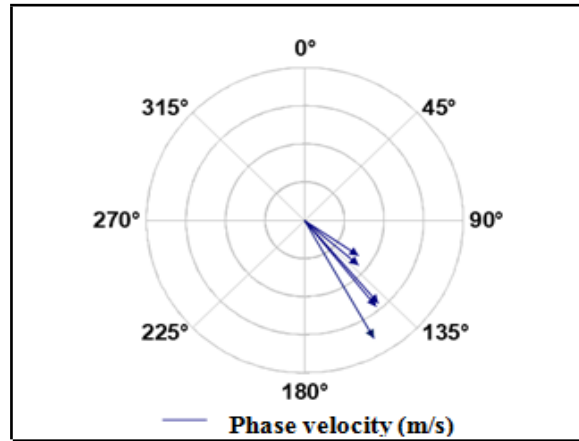
Figure 2: Compass graph showing wave velocities and direction of propagation- each circle denotes a velocity of 20 m/s.

      Figure 3 shows the impact of the atmospheric wind on the period of the waves. It reveals the difference between 180 the intrinsic period of the waves which lacks atmospheric impact and the observed period which is susceptible to the influence of the atmospheric winds. However, it can be seen that the winds accelerated almost all the gravity waves. The fluctuation in the period can be attributed to the variability of the horizontal winds. When the gravity wave is traveling anti-parallel to the wind direction, the second term on the left side of this equation $\omega_I = \omega_o - k_H . V_{GW}$ would become negative, consequently forcing the observed frequency to be smaller than the intrinsic frequency, this invariably results in 185 increased observed periods.
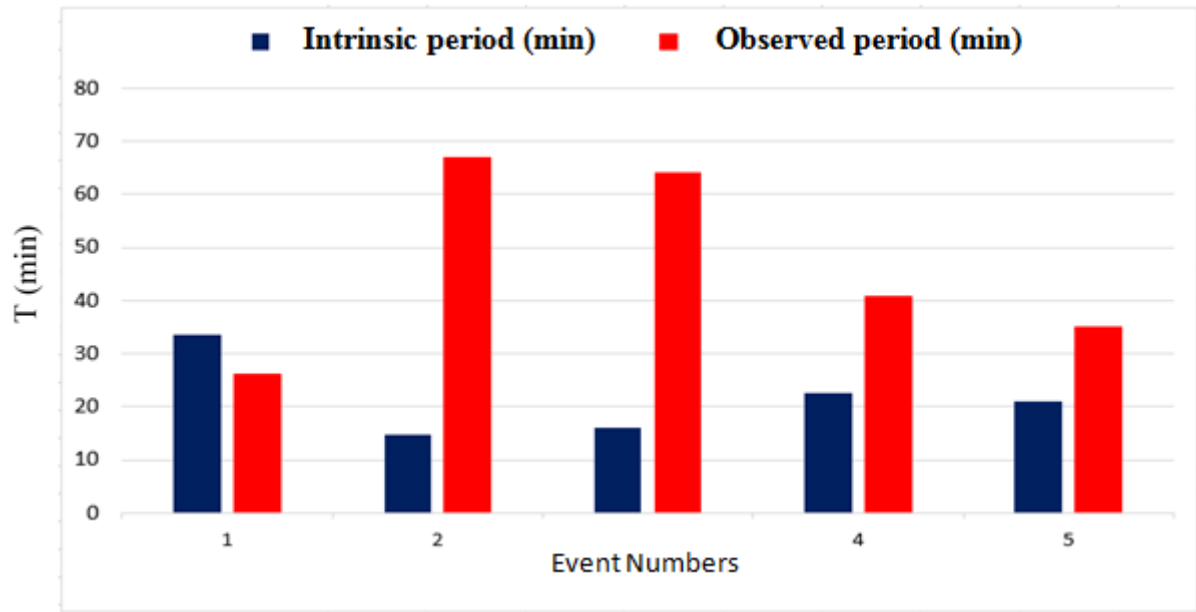
Figure 3: Bar chart graphs of intrinsic and observed periods.

4.2 Reverse ray-tracing

These 5 waves have different spectral characteristics and they were all observed at different times as well. Using the reverse ray tracing technique (RRT) to back trace these gravity waves from the point of observation in the airglow layer to their source of generation, we present the following results of the RRT analysis. During the backward tracing, we assumed critical levels are not encountered as explained in section 3.3.

The a-panels of Fig. (4-8) are the ray-paths as a function of the altitude and time and it describes the influence of various wind conditions on each GW event. The light blue line indicates the trajectory of the gravity wave under zero wind influence, while the black line shows the travel path of the wave under the HWM wind influence. This gave a better understanding of the roles played by the atmospheric winds in the traveling paths of GWs from the middle to the lower atmosphere. The blue and black shaded circles represents the time of generation of these waves under zero and modeled wind scenarios respectively. The dashed blue and solid black lines represents the trajectory of the waves under the zero winds and modeled winds conditions respectively.

The b-panels of Figure 4-8, however, describe the wave path as a function of longitude-latitude; thus providing a closer view of the exact generation point of these waves linearized over the map. The dark blue clouds represent the corresponding convective processes observed at the exact time that these gravity waves were detected. The black shaded triangle represents the precise location of the ASI at the OLAP.

Figure 4(b) shows a gravity wave propagating southeastward. Under the modeled wind conditions, this wave was generated at 17h00 UT of the same day, while under zero wind influence, it was triggered at 16h30 UT. Thus, the atmospheric winds were favorable as it accelerated the travel speed. The b-panel of Figure 4 zooms in on the actual source point of this wave. With a horizontal wavelength of 90 km, and phase velocity of 57.2 m/s, the reverse ray tracing result points to the source being in the northern region of the detection point (OLAP). Even though, the HWM-14 winds and zero winds are not equal, the gravity waves propagated through a similar path under both wind condition. Below 70 km, the GW propagates rapidly in the southeast direction which could be due to the strong winds.
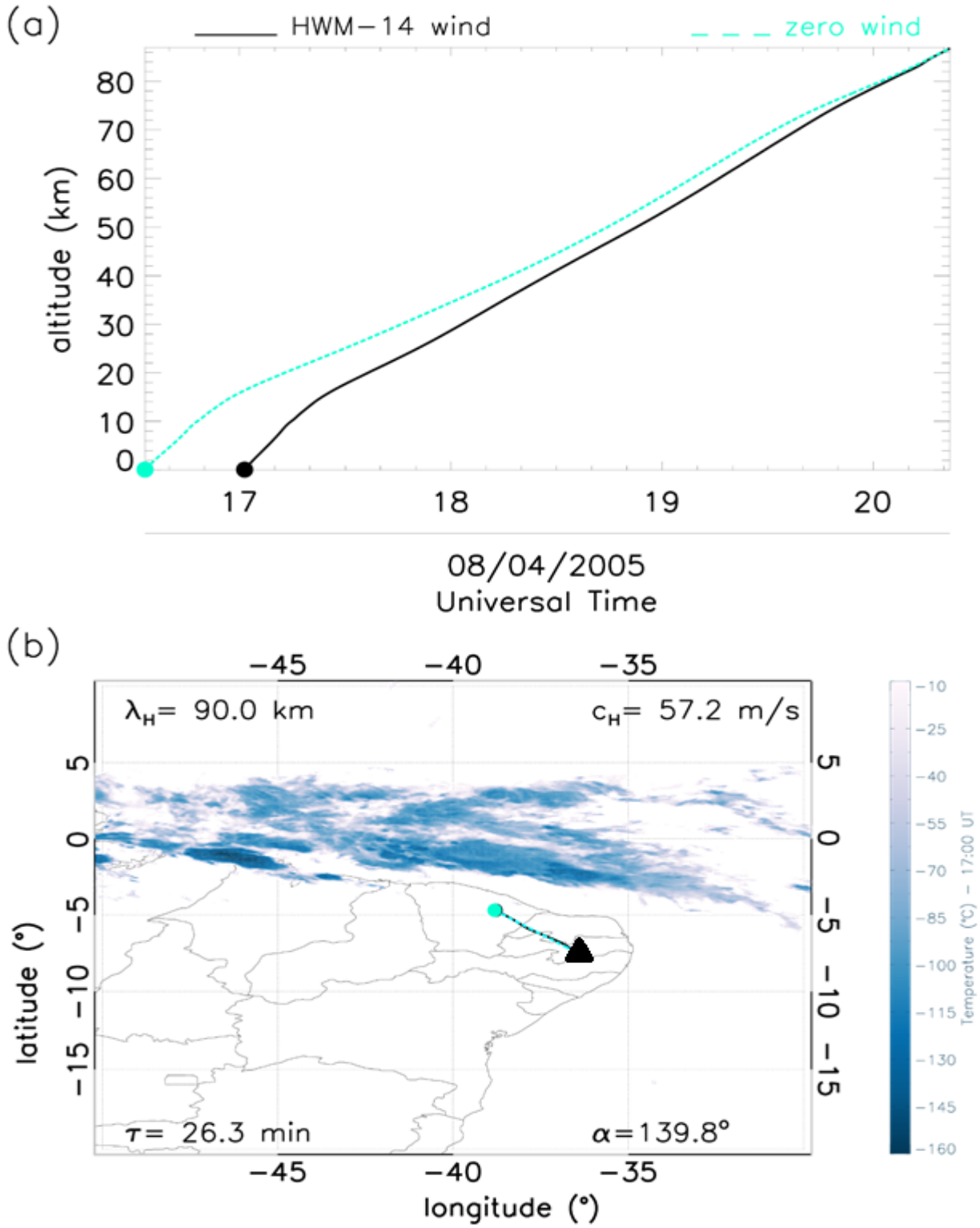
Figure 4: Reverse ray trace results for GW 1 (a-panels: Altitude as a function of time. Dashed blue and solid black lines show the ray paths for the zero winds and modeled winds respectively, and the time cross section with zero wind and modeled winds. (b-panels: Latitude-longitude cross section over convective cloud activities). Black and blue dots show the location of sources for zero winds and modeled winds respectively. The black triangle represents the exact location of the ASI, while the blue plumes represent convective activities in the region.

Similarly, the ray-tracing results show backward propagation of the second wave event detected at 21h33 UT in Figure 5(a). This shows a similar analysis when compared to the first wave event. However, this wave suffered greater wind acceleration ~12 hours as did GW_3 ~10 hours. Thus, just as in GW_1, both GW_4 and GW_5 were accelerated by the modeled winds just by ~ 2 hours and 1 hour respectively.
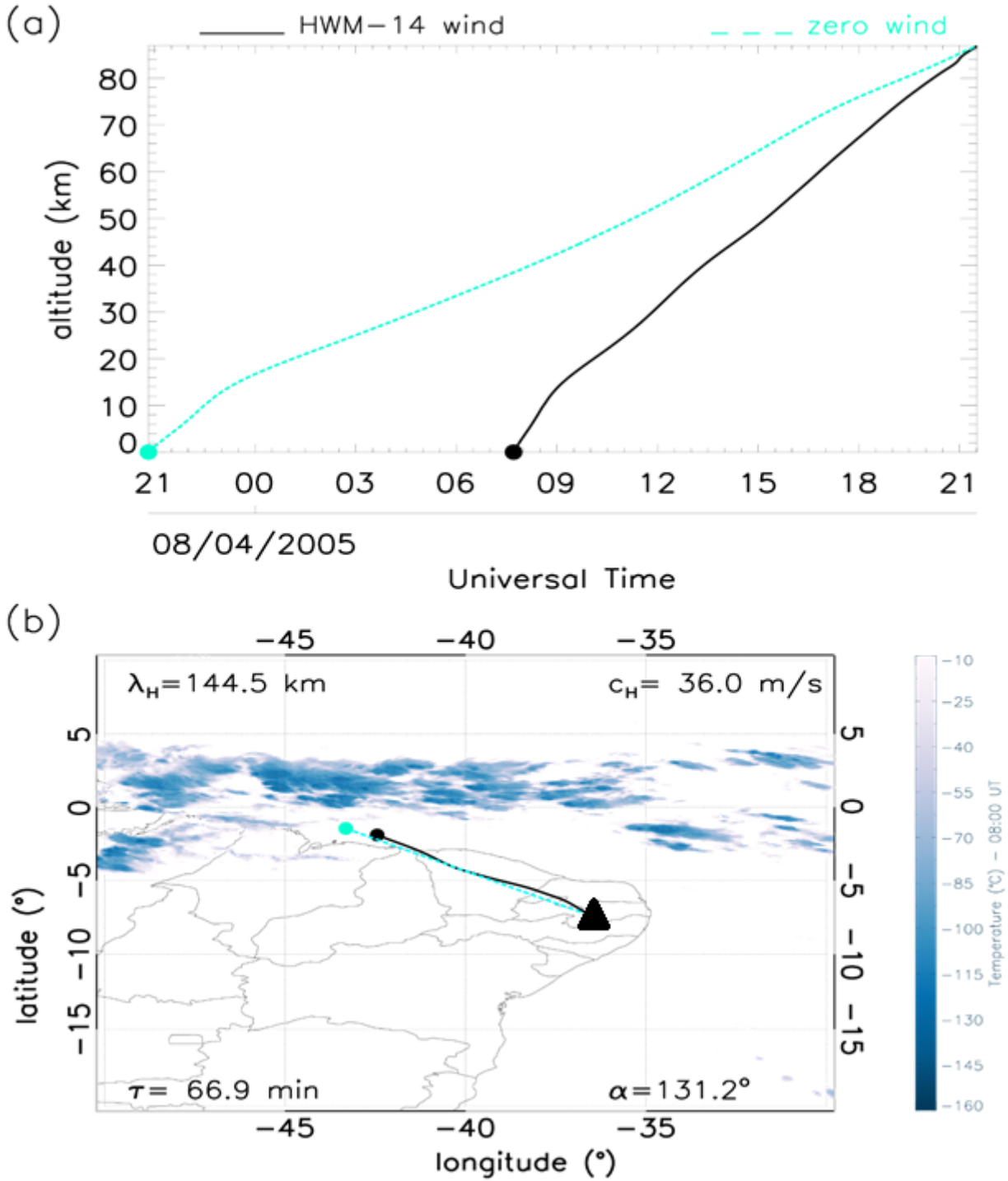
215

Figure 5: Same as in Figure 4 but for Event #2.

It was observed that the events 2, 3, 4, and 5 with a mean horizontal wavelengths of 140 km propagated more than ~1300 km from their source region. All these 4 events are believed to have originated from the same source due to the resemblance in their characteristics. In Event 1, in comparison to others, the bottom side of the convective sources (deep blue clouds) appear to be farther from the point where we traced the gravity wave source (black and blue dots). However, this particular wave is still linked to the convective processes as its source. According to Vadas and Fritts, 2009, the actual convective area is usually larger than the cloudy areas.
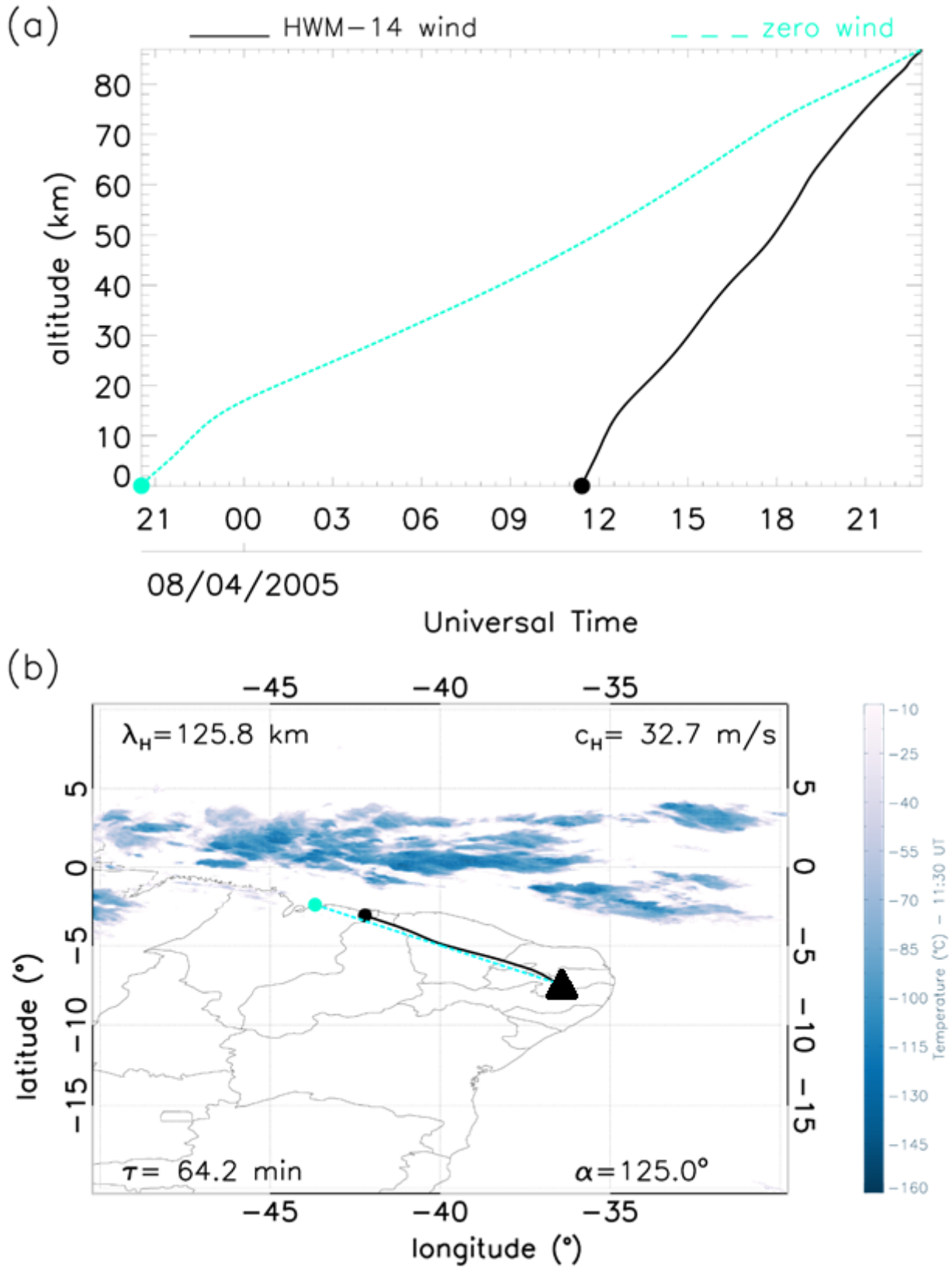
Figure 6: Same as Figure 4, but for the Event #3

Figures 4(b)-8(b) showed the ray paths for the wave events considering the normal and zero wind conditions. In the first panel of event 3, zero wind condition was applied, (blue line) and the modeled wind condition (black line) with a horizontal wavelength of 90 km, phase velocity of 57.2 m/s, propagating angle of 139.8°, 26.3-min period and a vertical wavelength of 90.2 km. It can be noticed in panel (a) of Event #3 that the GW attained the 87 km height for both wind 220conditions. A slight shift can be observed as there is similarity between both conditions.
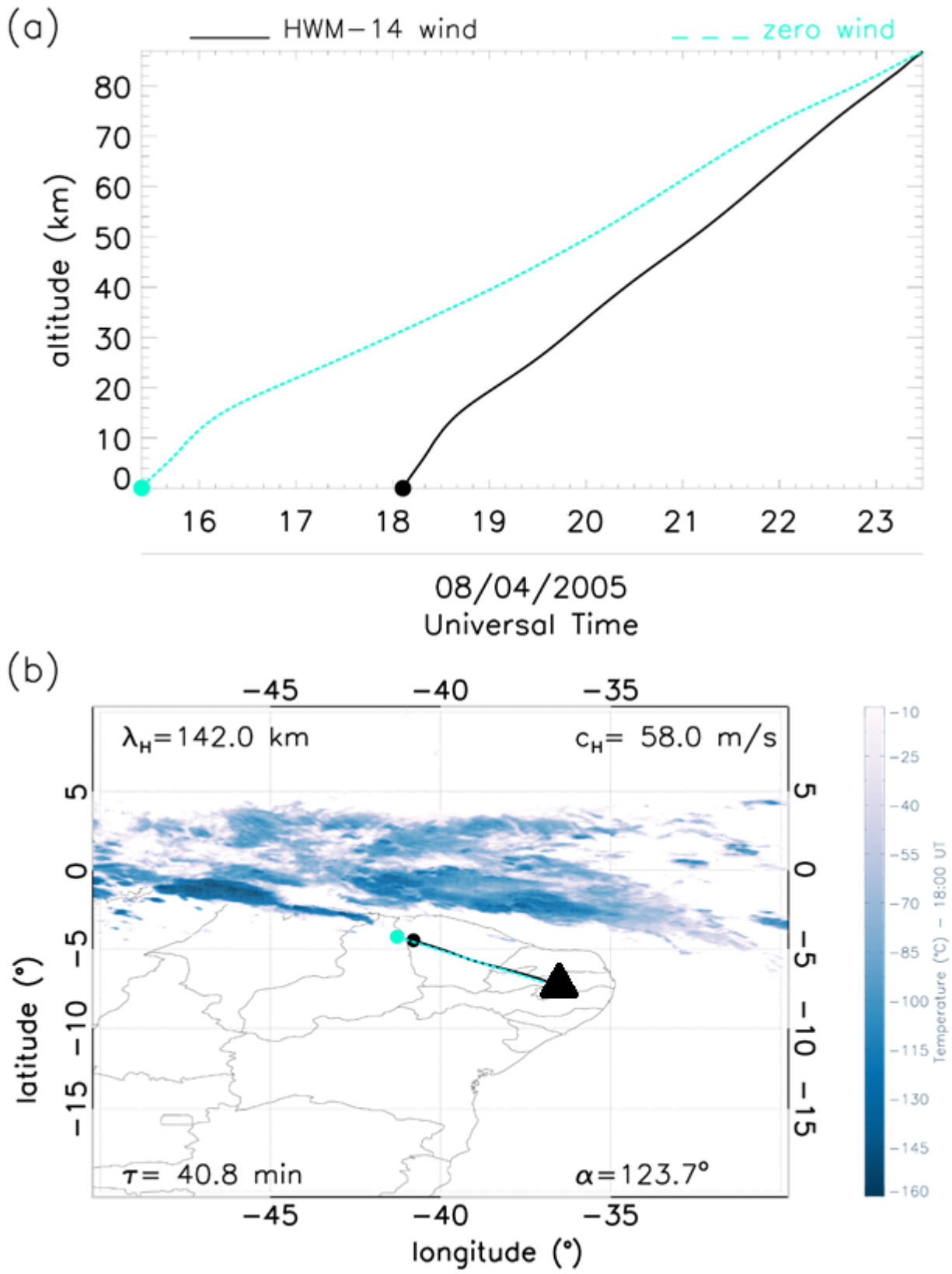
Figure 7: Same as Figure 4 but for Event #4.
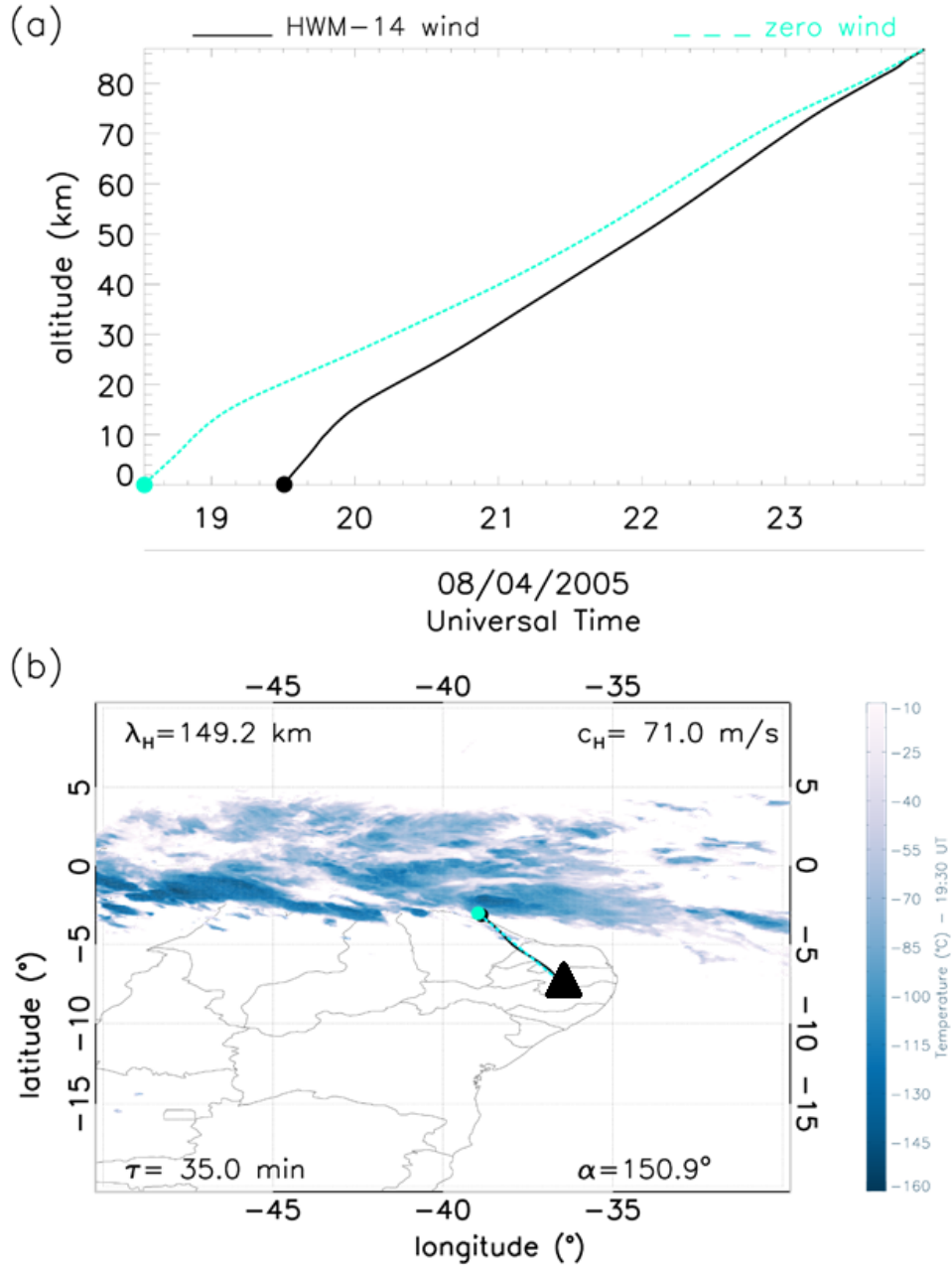
Figure 8: Same as Figure 5 but for event #5.

225   All the 5 wave events were reverse traced to some convection activities occurring in the northern region of the OLAP observatory. These have been identified as possible generators of these waves. One question is evident, why is the propagation direction of all the waves southeastward, since the ITCZ extends horizontally and covers the northern-region of the observatory? These results are in close agreement with previous results of different studies obtained at this laboratory (e.g., Medeiros et al., 2003 and Essien et al., 2018). It is expected that the gravity waves should propagate across all

230 directions in accordance to the location of the ITCZ. Thus, further investigation was done to explain this anisotropy phenomenon. To better understand the physical mechanism that is producing the anisotropy, blocking diagrams have been used to investigate the role of the wind in the filtering process of these gravity waves.

       Atmospheric winds are the default features of a real atmosphere. As these gravity waves propagate in the wind direction into the upper atmosphere, they would be susceptible to the Doppler's effect and critical level dissipation

235 (Bretherton, 1966). The critical level marks the region where the horizontal wind component annuls the wave's horizontal phase speed (Medeiros et al., 2003). This region is very important as it decides how and if a traveling wave would propagate further. To understand the anisotropy of these GWs, we apply the critical level theory of the atmospheric gravity

waves filtering (Fritts and Geller, 1976; Fritts, 1979). From Gossard and Hooke (1975) relation, the intrinsic frequency of the gravity wave under the influence of both horizontal wind components can be described by equation 4 below.

240 $$\omega_I = k \cdot (c - V)$$ (4)

where k is the magnitude of the horizontal wave vector, $\mathbf{V}$ represents the two horizontal wind components, and c is the horizontal phase speeds of the gravity waves. Equation (4) can also be re-expressed in terms of the zonal and meridional components. Further details can be found in the works of Medeiros et al. (2003), Campos et al. (2016) and Paulino et al. (2018). According to $cH = U cos \oslash + V sin \oslash$, where cH represents the phase speeds of these waves, U is the zonal

245 wind component and V is the meridional wind component, we constructed blocking diagrams using the azimuthal angles (ø). With input winds from the Horizontal Wind Model, we aimed to understand the wind filtering effects on the gravity waves, investigate why all the waves have a preferential propagation direction, and also to detect regions where the phase speed of the GW is ≤ the velocity of the winds. The results of the 3-D blocking diagrams are shown in the following figures.
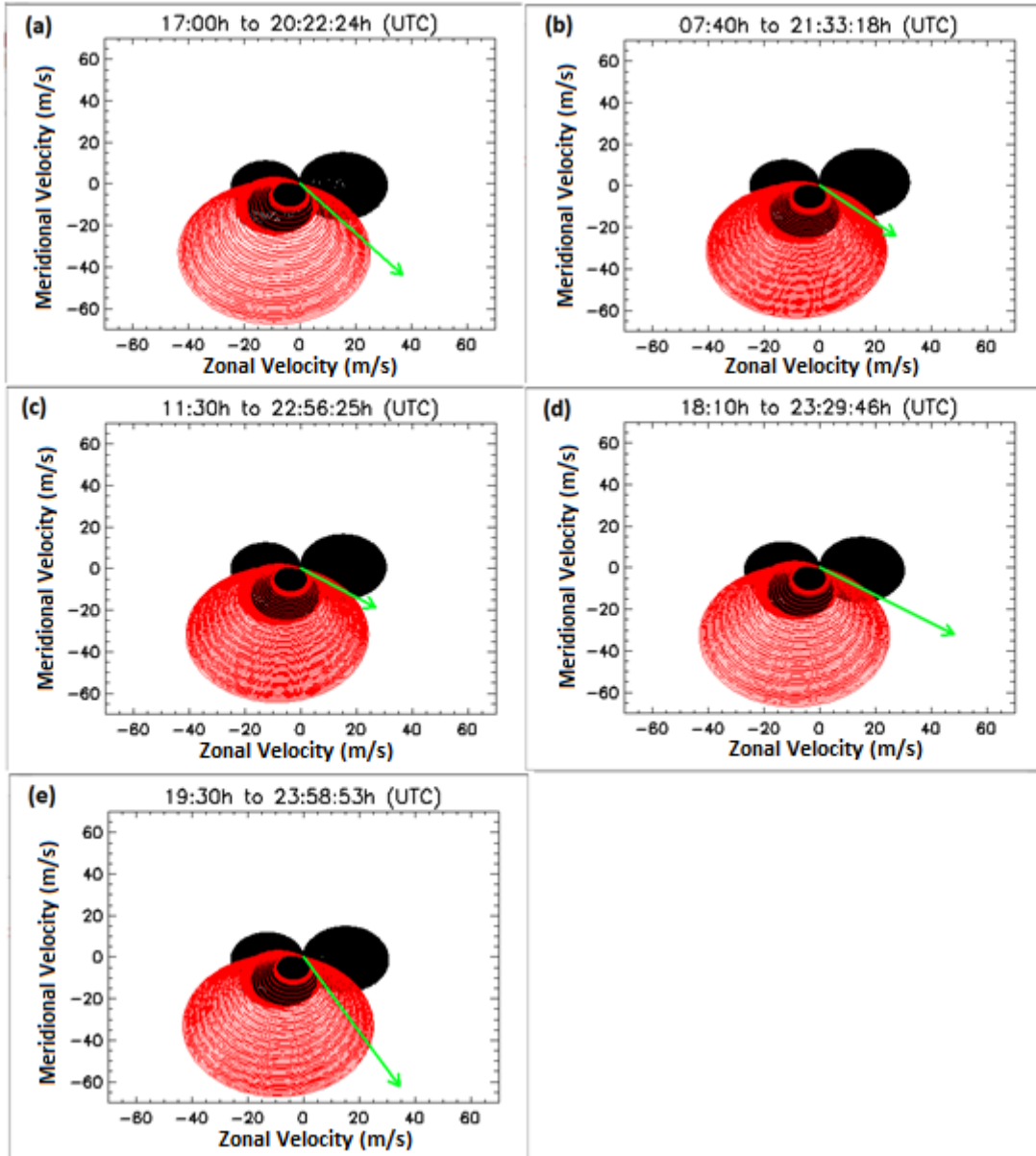
Figure 9: (a) Two-dimensional blocking diagrams for GW #1, (b) GW #2, (c) GW #3, (d) GW #4, and (e) GW #5 events observed at the OH layer (87 km). The green arrow depicts the magnitude and direction of the phase velocity of each gravity wave. The meshed region in red and black represents the magnitude and the direction of the restricted area for the propagation of the wave to the (OH) layer.

250   Constructing a polar chart as a function of the azimuthal angles and phase speeds using the wind data from HWM and the SkiYMET radar, we show where the phase speeds of these gravity waves equaled the wind speed of the background. The critical levels were projected into the blocking diagram showing for each horizontal wind speed and azimuths of the corresponding GWs. If the phase speed of the GW is trapped in the blocking lines, it represents that the wave is prohibited to propagate upwards.

255   The above blocking diagram allows the detection of regions where $\omega_I \leq 0$ on the night of 08 April 2005 for the OH emission layer. Every circle in this diagram shows the critical level of the vertical propagation of these waves. The red and black mesh signify the measured and modeled wind components respectively while the green arrow represents the magnitude and direction of the detected GW. The theory of filtering process of gravity waves disallows waves propagating into the shaded region due to the effect of the critical levels (Paulino et al. 2018).

260   Similarly, we observed that the phase velocity of all the GW events were indeed greater in magnitude than the blocking area. They had strong speed and momentum, enough to escape and propagate through the critical levels easily. It is important to note the main contributions to the blocking area were due to the measured wind in the mesosphere and lower thermosphere, making this analysis strongly confident.

   Thus, these detected waves avoided and escaped absorption in the forbidden regions by traveling at these
265 interesting angles. The anisotropy of these waves furthermore compels the source location of the wave to be in the Northwest because the location of this wave source played a key role in this preferential traveling (Fritts et al., 2008; Campos et al.; 2016). The sources of these waves were identified as the convective processes in the ITCZ zone.

5. Conclusions

   Using OH airglow images captured by the ASI at São João do Cariri, we investigated the sources of some gravity
270 waves observed on the night of 08 April 2005 in the OH airglow layer. Using the spectral analyzing method, we obtained the characteristics of 5 major gravity events with horizontal wavelengths concentrated between 90 km and 149 km. The phase speeds were distributed between the range of 32 m/s and 71 m/s, and the observed periods extended from 26 min to 67 min. These waves presented spectral characteristics that are very compatible with waves previously observed in the same site. In addition, southeast propagation suggested possible sources in the northwest of the observatory.

275   Focusing on the possible sources of these waves, we back-traced the trajectory of each of these waves from the OH layer $\left(87\,km\right)$ into the troposphere using the meteor radar wind data, the HWM model winds, and zero winds. We found out that the RRT put the source as active convective processes (in the ITCZ) in the northwest of the laboratory as shown in the back tracing results presented above. However, the ITCZ was extended by a long strip in the northern part of the observatory which suggested generation of other GWs that should have been observed in the south and southwest of the
280 observatory. Thus, the construction of blocking diagrams showed that only the spectrum of waves with propagation to the southeast were able to propagate vertically to altitudes of the OH layer. Therefore, the filtering effect of gravity waves was decisive for explaining the presence of observed waves propagating to the Southeast.

Data availability: All sky image data used in the course of this study can be requested from Aerolume (UFCG) or Lume (INPE) Groups by mailing igo.paulino@df.ufcg.edu.br.

285 *Author contributions*: OD-I has written the manuscript. IP has revised the manuscript and supervised the research. CAOBF has calculated the deep cloudy convection over the OLAP area. ARP has provided wind measurements from the meteor radar, and revised the manuscript. RAB and AFM have revised the full text. CMW has provided the spectral analysis for the observed gravity waves.

Competing interests: All the authors declare that they do not have any competing interests.

290 *Acknowledgements.* O. Dare-Idowu sincerely thanks the Coodernação de Aperfeiçoamento de Pessoal de nível Superior for the scholarship during her Masters program in UFCG. I. Paulino gives special gratitude to the Conselho Nacional de Desenvolvimento Científico e Tecnológico (CNPq) for their financial support (303511/2017-6) and UFCG for giving their strong financial support during the presentation of this work at the 27th IUGG Scientific Assembly.

References

295 Bretherton, F. P.: The propagation of groups of internal gravity waves in a shear flow, Journal of the Royal Meteorological Society, 92(394), 466–480, https://doi.org/10.1002/qj.49709239403, 1966.

Brown, L. B., Gerrard, A. J., Meriwether, J. W., and Makela, J. J.: All-sky imaging observations of mesospheric fronts in OI 557.7 nm and broadband OH airglow emissions: Analysis of frontal structure, atmospheric background conditions, and potential sourcing mechanisms, Journal of Geophysical Research D: Atmospheres, 109(19), 300 https://doi.org/10.1029/2003JD004223, 2004.

Campos J. A. V., Paulino, I., Wrasse, C. M., Medeiros, A. F., Paulino, A. R., and Buriti, R. A.: Observations of small-scale gravity waves in the equatorial upper mesosphere, Revista Brasileira de Geofisica, 34(4), https://doi.org/10.22564/rbgf.v34i4.876, 2016.

Clemesha, B. and Batista, P.: Gravity waves and wind-shear in the MLT at 23°S, Advances in Space Research, 41, 1472 – 305 1477, https://doi.org/https://doi.org/10.1016/j.asr.2007.03.085, 2008.

Drob, D. P., Emmert, J. T., Crowley, G., Picone, J. M., Shepherd, G. G., Skinner, W., Hays, P., Niciejewski, R. J., Larsen, M., She, C. Y., Meriwether, J. W., Hernandez, G., Jarvis, M. J., Sipler, D. P., Tepley, C. A., O'Brien, M. S., Bowman, J. R., Wu, Q., Murayama, Y.,Kawamura, S., Reid, I. M., and Vincent, R. A.: An empirical model of the Earth's horizontal wind fields: HWM07, Journal of Geophysical Research (Space Physics), 113, 12 304, https://doi.org/10.1029/2008JA013668, 310 2008.

Egito, Fabio & Arlen Buriti, Ricardo & Medeiros, A & Takahashi, Hisao. (2018). Ultrafast Kelvin waves in the MLT airglow and wind, and their interaction with the atmospheric tides. Annales Geophysicae. 36. 231-241. https://doi.org/10.5194/angeo-36-231-2018.

Essien P., E., Paulino, I., Wrasse, C. M., Campos, J. A. V., Paulino, A. R., Medeiros, A. F., and Buriti, R. A.: Seasonal 315 characteristics of small- and medium-scale gravity waves in the mesosphere and lower thermosphere region over Brazilian equatorial sector, Annales Geophysicae, (Submetid), 1–26, https://doi.org/10.5194/angeo-36-899-2018, 2018.

Fritts, D. C.: The excitation of radiating waves and Kelvin-Helmholtz instabilities by the gravity wave-critical level interaction, J. Atmos. Sci., 36, 12–23, https://doi.org/10.1175/1520-0469(1979)036<0012:TEORWA>2.0.CO;2, 1979.

Fritts, D. C. and Alexander, M. J.: Gravity wave dynamics and effects in the middle atmosphere, Reviews of Geophysics, 41, 320 n/a–n/a, https://doi.org/10.1029/2001RG000106, 1003, 2003.

Fritts, D. C. and Geller, M. A.: Viscous stabilization of gravity wave critical level flows, J. Atmos. Sci., 33, 2276– 2284, https://doi.org/10.1175/1520-0469(1976)033<2276:VSOGWC>2.0.CO;2, 1976.

Fritts, D. C. and Luo, Z. (1993). Gravity wave forcing in the middle atmosphere due to reduced ozone heating during a solar eclipse. Journal of Geophysical Research, 98(D2), 3011– 3021. https://doi.org/10.1029/92JD02391

325 Fritts, D. C., Vadas, S. L., Riggin, D. M., Abdu, M. A., Batista, I. S., Takahashi, H., Medeiros, A., Kamalabadi, F., Liu, H.-L., Fejer, B. G., and Taylor, M. J.: Gravity wave and tidal influences on equatorial spread F based on observations during the Spread F Experiment (SpreadFEx), Ann. Geophys., 26, 3235–3252, https://doi.org/10.5194/angeo-26-3235-2008, 2008

Gossard, E. and Hooke, W.: Waves in the atmosphere: atmospheric infrasound and gravity waves- their generation and propagation, Elsevier Scientific Publishing Co., 1975.

330 Hecht, J. H., Walterscheid, R. L., and Ross, M. N.: First measurements of the two-dimensional horizontal wave number spectrum from CCD images of the nightglow, Journal of Geophysical Research, 99(A6), 11449, https://doi.org/10.1029/94JA00584, 1994.

Hocking, W. K., Fuller, B., and Vandepeer, B.: Real-time determination of meteor-related parameters utilizing modern digital technology, Journal of Atmospheric and Solar-Terrestrial Physics, 63(2–3), 155–169, https://doi.org/10.1016/S1364-
335 6826(00)00138-3, 2001.

Krasovskij, V. I. & Šefov, N. N. 1965. Airglow. https://doi.org/10.1007/BF00173881

Marlton, G. J., Williams, P. D., and Nicoll, K. A.: On the detection and attribution of gravity waves generated by the 20 March 2015 solar eclipse, https://doi.org/10.1098/rsta.2015.0222, 2016.

Medeiros, A. F., Taylor M. J., Takahashi, H., Batista, P. P., and Gobbi, D.: An investigation of gravity wave activity in the
340 low-latitude upper mesosphere: Propagation direction and wind filtering, Journal of Geophysical Research: Atmospheres, 108, https://doi.org/10.1029/2002JD002593, 2003.

Medeiros, A. F., Takahashi, H., Buriti, R. A., Fechine, J., Wrasse, C. M., and Gobbi, D.: MLT gravity wave climatology in the South America equatorial region observed by airglow imager, Annales Geophysicae, 25, 399–406, https://doi.org/10.5194/angeo-25-399-2007, 2007.

345 Mertens, C. J., Mlynczak, M. G., López-Puertas, M., Wintersteiner, P. P., Picard, R. H., Winick, J. R., Gordley, L. L., and Russell III, J. M.: Retrieval of mesospheric and lower thermospheric kinetic temperature from measurements of CO_2 15 μm Earth Limb Emission under non-LTE conditions, Geophysical Research Letters, 28, 1391–1394, https://doi.org/10.1029/2000GL012189, 2001.

Nyassor P. K., Buriti, R. A., Paulino, I., Medeiros, A. F., Takahashi, H., Wrasse, C. M., and Gobbi, D.: Determination of
350 gravity wave parameters in the airglow combining photometer and imager data. Annales Geophysicae, 36(3), 705–715, https://doi.org/10.5194/angeo-36-705-2018, 2018.

Paulino, A., Batista, P., Lima, L., Clemesha, B., Buriti, R., and Schuch, N.: The lunar tides in the mesosphere and lower thermosphere over Brazilian sector, Journal of Atmospheric and Solar-Terrestrial Physics, 133, 129 – 138, https://doi.org/10.1016/j.jastp.2015.08.011, 2015.

355 Paulino, A. R., Batista, P. P., and Batista, I. S.: A global view of the atmospheric lunar semidiurnal tide, Journal of Geophysical Research: Atmospheres, 118, 13,128–13,139, https://doi.org/10.1002/2013JD019818, 2013.

Paulino, I., Medeiros, A., Buriti, R., Sobral, J., Takahashi, H., and Gobbi, D.: Optical observations of plasma bubble westward drifts over Brazilian tropical region, Journal of Atmospheric and Solar-Terrestrial Physics, 72, 521 – 527, https://doi.org/10.1016/j.jastp.2010.01.015, 2010.

360 Paulino, I., Takahashi, H., Vadas, S., Wrasse, C., Sobral, J., Medeiros, A., Buriti, R., and Gobbi, D.: Forward ray-tracing for medium-scale gravity waves observed during the {COPEX} campaign, Journal of Atmospheric and Solar-Terrestrial

Physics, 90-91, 117 – 123, https://doi.org/10.1016/j.jastp.2012.08.006, recent Progress in the Vertical Coupling in the Atmosphere-Ionosphere System, 2012.

Paulino, I., Moraes, J. F., Maranhão, G. L., Wrasse, C. M., Buriti, R. A., Medeiros, A. F., Paulino, A. R., Takahashi, H.,
365 Makela, J. J., Meriwether, J. W., and Campos, J. A. V.: Intrinsic parameters of periodic waves observed in the OI6300 airglow layer over the Brazilian equatorial region, Annales Geophysicae, 36, 265–273, https://doi.org/10.5194/angeo-36-265-2018, https://www.ann-geophys.net/36/265/2018/, 2018.

Picone, J. M., Hedin, A. E., Drob, D. P., and Aikin, A. C.: NRLMSISE-00 empirical model of the atmosphere: Statistical comparisons and scientific issues, J. Geophys. Res., 107, 1468, 0148-0227, 2002.

370 Plougonven, R., Jewtoukoff, V., Cámara, A. d. l., Lott, F., and Hertzog, A.: On the Relation between Gravity Waves and Wind Speed in the Lower Stratosphere over the Southern Ocean, Journal of the Atmospheric Sciences, 74, 1075–1093, https://doi.org/10.1175/JAS-D-16-0096.1, 2017.

Pramitha, M., Venkat Ratnam, M., Taori, A., Krishna Murthy, B. V., Pallamraju, D., and Vijaya Bhaskar Rao, S.: Identification of gravity wave sources using reverse ray tracing over Indian region, https://doi.org/10.5194/acpd-14-19587-
375 2014, 2014.

PRESS, W. H. Numerical recipes 3rd edition: The Art of scientific computing. 3. ed. New York [etc.]: Cambridge University Press, 2007. ISBN 0521880688. 118

Sarkar, S., and Scotti, A.: Topographic Internal Gravity Waves to Turbulence, Annual Review of Fluid Mechanics, 49(1), 195–220. https://doi.org/10.1146/annurev-fluid-010816-060013, 2017.

380 Sivakandan, M., Paulino, I., Taori, A., and Niranjan, K.: Mesospheric gravity wave characteristics and identification of their sources around spring equinox over Indian low latitudes, 9(1), 93–102, https://doi.org/10.5194/amt-9-93-2016, 2016.

Sivjee G. G.,Airglow hydroxyl emissions,Planetary and Space Science,Volume 40, Issues 2–3,1992, Pages 235-242,ISSN 0032-0633, https://doi.org/10.1016/0032-0633(92)90061-R.

Taylor M. J., Pautet P.D, Medeiros A., Buriti R., Fechine J., Fritts D., Vadas S., Takahashi H. & Sao Sabbas F. 2009:
385 Characteristics of mesospheric gravity waves near the magnetic equator, Brazil, during the SpreadFEx campaign. Annales Geophysicae, 27: 461–472.

Vadas, S. L. and Fritts, D. C.: Thermospheric responses to gravity waves: Influences of increasing viscosity and thermal diffusivity, Journal of Geophysical Research: Atmospheres, 110, https://doi.org/10.1029/2004JD005574, 2005.

Vadas, S. L.: Horizontal and vertical propagation and dissipation of gravity waves in the thermosphere from lower
390 atmospheric and thermospheric sources, Journal of Geophysical Research: Space Physics, 112, https://doi.org/10.1029/2006JA011845, 2007.

Vadas, S. L., and Liu, H. (2009), Generation of large-scale gravity waves and neutral winds in the thermosphere from the dissipation of convectively generated gravity waves, J. Geophys. Res., 114, A10310, https://doi.org/10.1029/2009JA014108.

Vadas, S. L. and Fritts, D. C.: Reconstruction of the gravity wave field from convective plumes via ray tracing, Annales
395 Geophysicae, 27, 147–177, https://doi.org/10.5194/angeo-27-147-2009, 2009.

Vadas, S. L., Taylor, M. J., Pautet, P.-D., Stamus, P. A., Fritts, D. C., Liu, H.-L., São Sabbas, F. T., Rampinelli, V. T., Batista, P., and Takahashi, H.: Convection: the likely source of the medium-scale gravity waves observed in the OH airglow layer near Brasilia, Brazil, during the SpreadFEx campaign, Annales Geophysicae, 27, 231–259, https://doi.org/10.5194/angeo-27-231-2009, 2009.

400 Vargas, F., D. Gobbi, H. Takahashi, and L. M. Lima (2009), Gravity wave amplitudes and momentum fluxes inferred from OH airglow intensities and meteor radar winds during SpreadFEx, Ann. Geophys., 27(6), 2361– 2369, https://doi.org/10.5194/angeo-27-2361-2009.

Wallace L., Chamberlain J.W.: Excitation of O2 atmospheric bands in the aurora, Planetary and Space Science, Volume 2, Issue 1, 1959, Pages 60-70, ISSN 0032-0633, https://doi.org/10.1016/0032-0633(59)90060-1.

405 Wrasse, C. M., Nakamura, T., Takahashi, H., Medeiros, A. F., Taylor, M. J., Gobbi, D., Denardini, C. M., Fechine, J., Buriti, R. A., Salatun, A., Suratno, A., Achmad, E., and Admiranto, A. G.: Mesospheric gravity waves observed near equatorial and low and middle latitude stations: wave characteristics and reverse ray tracing results, Annales Geophysicae, 24, 3229–3240, https://doi.org/10.5194/angeo-24-3229-2006, 2006.